Understanding the kinetics and mechanism of thermal cheletropic elimination of N2 from (2,5-dihydro-1H-pyrrol-1-ium-1-ylidene) amide using RRKM and ELF theories

DOI: 10.1007/s11164-016-2716-3
Handle: http://hdl.handle.net/1942/23201

Understanding the kinetics and mechanism of thermal cheletropic elimination of N_2 from (2,5-dihydro-1*H*-pyrrol-1-ium-1-ylidene) amide using RRKM and ELF theories

Ehsan Zahedi[a,*], Majid Mozaffari[a], Farzaneh Shahsavar[a], Abolfazl Shiroudi[b], Michael S. Deleuze[c]

[a] *Chemistry Department, Shahrood Branch, Islamic Azad University, Shahrood, Iran*

[b] *Young Researchers and Elite Club, East Tehran Branch, Islamic Azad University, Tehran, Iran*

[c] *Center of Molecular and Materials Modelling, Hasselt University, Agoralaan, Gebouw D, B-3590 Diepenbeek, Belgium.*

ABSTRACT

The cheletropic elimination process of N_2 from (2,5-dihydro-1H-pyrrol-1-ium-1-ylidene) amide ($C_4H_6N_2$) has been studied computationally using density functional theory, along with the M06-2*x*/aug-cc-pVTZ level of theory. The calculated energy profile has been supplemented with calculations of kinetic rate constants using transition state theory (TST) and statistical Rice–Ramsperger–Kassel–Marcus (RRKM) theory. This elimination process takes place spontaneously with an activation energy around 33 kJ/mol. Pressure dependence of the rate constants revealed that the TST approximation breaks down and fall-off expression is necessary for the kinetic modeling. At temperatures ranging from 240 to 360 K and atmospheric pressure, the unimolecular rate constant is evaluated from RRKM theory as $k^{1.0\,\mathrm{atm}}_{(240-360\,\mathrm{K})} = 1.0249\times10^{12}\times \mathrm{e}^{-\frac{33.11\,\mathrm{kJ/mol}}{RT}}$ s^{-1}. Bonding changes along the reaction coordinate have been studied using bonding evolution theory. Electron localization function topological analysis reveals that the cheletropic elimination is characterized topologically by four successive structural stability domains (SSDs). Breaking of C–N bonds (Rx=0.1992 $amu^{1/2}$Bohr) and the other selected points separating the SSDs along the reaction coordinate occur in the vicinity of the transition state.

Keywords: Cheletropic elimination; DFT; TST; RRKM theory; BET; ELF.

[*] Corresponding author. Tel: +98 9122733755; Fax: +98 23 32344634

E-mail addresses: e_zahedi1357@yahoo.com; e_zahedi@iau-shahrood.ac.ir

Introduction

A reaction mechanism describes in detail how bond breaking and bond forming processes take place at the microscopic level along the channel connecting reactants to products through the corresponding transition structure (TS). A widely used approach to obtain a robust quantitative definition of chemical bonding is based on the idea of bond basin population derived from the electron localization function (ELF) theory proposed by Becke and Edgecombe [1], which has been extensively developed by Silvi and Savin [2]. This method has been extensively applied recently to study the molecular mechanisms of a wide range of organic reactions, such as Cope rearrangements, Diels-Alder, 1,3-dipolar and other cycloadditions, the Friedel-Crafts reaction, Staudinger reaction [3-18]. Cycloaddition reactions in particular have been extensively studied by Domingo and coworkers. Domingo [3, 19, 20] believes that breaking of the C=C double bonds and formation of the new C–C single bonds in the Diels-Alder reaction between butadiene and ethylene is non-concerted and formation of the C–C single bonds takes place through the C to C coupling between the generated pseudoradical centers due to the breaking of C=C double bonds. Similarly, the 1,3-dipolar cycloaddition reaction of fulminic acid and acetylene has been studied by Polo *et al.* [5]. They found that in the first step, C–C single bond formation takes place via a C to C coupling between the generated pseudoradical centers and finally the ring closure arises due to a dative process involving sharing of the lone pair of the oxygen atoms toward a carbon atom of acetylene. In spite of the fact that the reaction mechanisms of a number of pericyclic reactions have been studied using the ELF method, surprisingly little attention has been paid so far to the elucidation of the molecular mechanisms of cheletropic reactions. According to the Woodward-Hoffmann rules, the cheletropic reaction is a cycloaddition across the terminal atoms of a fully conjugated system involving the formation of two new σ bonds to a single atom in a concerted process. Elimination of simple stable molecules such as CO, N_2, N_2O and SO_2 from an unsaturated ring is often referred to as a cheletropic extrusion or elimination process [21] (see Scheme 1). Cheletropic extrusion is one of the most frequently studied examples of unimolecular thermal elimination reactions.

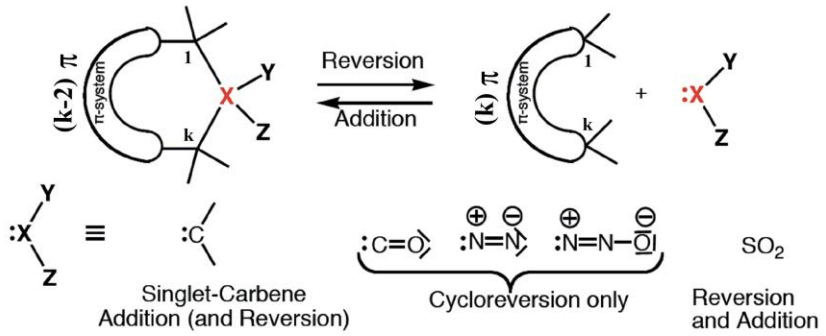

Scheme 1

The pressure-dependent kinetics of the thermal unimolecular decarbonylation of 3,5-cycloheptadienone (CHD), 3-cyclopentenone (CPE) and norbornenone (BCH) has been experimentally studied using shock tube and continuous waveform CO probe laser by Buxton *et al.* [22] A non-linear least-squares fitting of the pressure-dependent kinetic data lead to the following Arrhenius expressions:

$$k^{612\,\mathrm{Torr}}_{(1072\text{–}1268\,\mathrm{K})}(\mathrm{CHD}) = 10^{13.9\pm0.2} \times \mathrm{e}^{-\frac{207\pm10\ \mathrm{kJ/mol}}{RT}} \quad \mathrm{s}^{-1}$$

$$k^{\infty}_{(1140\text{–}1170\,\mathrm{K})}(\mathrm{CHD}) = 10^{16.2\pm0.8} \times \mathrm{e}^{-\frac{255\pm10\ \mathrm{kJ/mol}}{RT}} \quad \mathrm{s}^{-1}$$

$$k^{611\,\mathrm{Torr}}_{(1031\text{–}1327\,\mathrm{K})}(\mathrm{CPE}) = 10^{12.2\pm0.2} \times \mathrm{e}^{-\frac{169\pm6\ \mathrm{kJ/mol}}{RT}} \quad \mathrm{s}^{-1}$$

$$k^{\infty}_{(1150\text{–}1190\,\mathrm{K})}(\mathrm{CPE}) = 10^{13.8\pm0.3} \times \mathrm{e}^{-\frac{194\pm10\ \mathrm{kJ/mol}}{RT}} \quad \mathrm{s}^{-1}$$

$$k^{742\,\mathrm{Torr}}_{(721\text{–}851\,\mathrm{K})}(\mathrm{BCH}) = 10^{13.9\pm1.4} \times \mathrm{e}^{-\frac{138\pm10\ \mathrm{kJ/mol}}{RT}} \quad \mathrm{s}^{-1}$$

$$k^{\infty}_{(721\text{–}851\,\mathrm{K})}(\mathrm{BCH}) = 10^{14.2\pm0.4} \times \mathrm{e}^{-\frac{146\pm6\ \mathrm{kJ/mol}}{RT}} \quad \mathrm{s}^{-1}$$

Fall-off curve results indicated that, at atmospheric pressure and the lower pressures of the troposphere, the rates of decarbonylation of CHD and BCH are in the fall-off realm. A series of eight thermal cheletropic decarbonylation has been studied theoretically by Birney *et al.* [23] Their results indicate that reaction pathways and activation energies depend on the molecular orbital topology. They also showed that two orbital disconnections are sufficient to allow a reaction to be pseudopericyclic and to have an approximately planar transition structure. The cheletropic reactions of 1,3-dienes with sulfur dioxide have been extensively investigated experimentally by Isaacs *et al.*, [24] and theoretically by Suárez *et al.* [25] Isaacs and co-workers observed that an

electron-withdrawing group can reduce the activity of the diene, and a two-step mechanism was proposed based on theoretical results. Cheletropic extrusion of N_2 from (2,5-dihydro-1*H*-pyrrol-1-ium-1-ylidene) amide ($C_4H_6N_2$) has been experimentally studied by Lemal and McGregor [26]. They showed that the reaction of 3-pyrroline **1** with nitrohydroxylamine gives rise to the diazene intermediate **2**, in which the elimination of nitrogen can occur in high yield according to a concerted process (see Scheme 2).

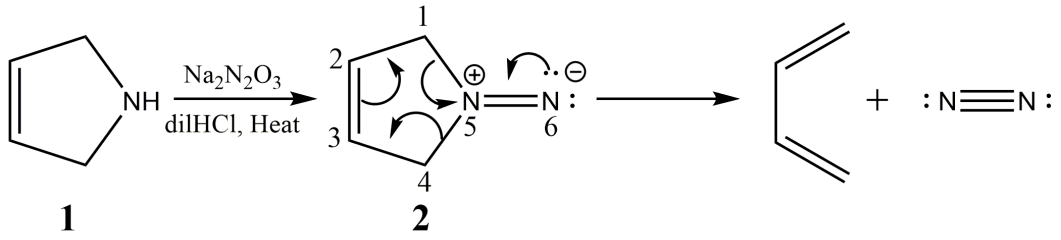

Scheme 2

Despite its apparent simplicity, the kinetics and nature of the reaction mechanism of cheletropic extrusion of N_2 from (2,5-dihydro-1*H*-pyrrol-1-ium-1-ylidene) amide ($C_4H_6N_2$) have not been investigated so far, and will be the subject of the present study. To this purpose, kinetic rate constants in the high pressure limit will be supplied by means of transition state theory (TST) [27-29], and their fall-off behavior at lower pressures will be studied using statistical Rice–Ramsperger–Kassel–Marcus (RRKM) theory [30-33]. A topological analysis of bonding changes along the reaction using the electron localization function approach is implemented in order to establish which molecular mechanism is associated with this reaction.

Theory and computational details

All electronic structure calculations that are discussed in this research have been done using the Gaussian 09 package of programs [34]. Geometry optimizations have been performed using the GEDIIS [35] optimizer of the Berny algorithm along with the M06-2*x* density functional of Zhao and Truhlar [36,37], in conjunction with Dunning's correlation-consistent basis set of triple-ζ quality augmented with diffuse functions (aug-cc-pVTZ basis set) [38]. The nature of all identified stationary points has been

verified according to calculations of harmonic vibrational frequencies at the same level of theory as the geometry optimization. Intrinsic reaction coordinate (IRC) analysis has been carried out in both directions (forward and backward) along the reaction path to verify whether the located transition state structure connects to the corresponding reactant and products, using the Hessian based predictor corrector (HPC) integrator algorithm [39-41].

Rate constants for the unimolecular reaction have been obtained in the high pressure limit at temperatures equal to 300, 500, 700, and 900 K, using standard transition state theory [42]:

$$k_{\mathrm{TST}}(T) = \frac{\sigma k_{\mathrm{B}} T}{h} \times \frac{Q^{\neq}}{Q_{\mathrm{R}}} \times \exp\left(-\frac{E^{\neq}}{\mathrm{k_B} T}\right) \tag{1}$$

where k_{B} is Boltzmann's constant, T is the absolute temperature, h is Planck's constant and $E^{\neq}$ is the activation energy, defined as the difference in zero-point corrected potential energy between the transition state and the reactant. $Q^{\neq}$ and Q_{R} denote the canonical partition function per unit volume of the TS and the reactant, respectively, without rotational symmetry numbers. Reaction symmetry number σ =1 is taken into consideration according to the C_1 point groups of symmetries of the reactant and the transition state. Kinetic rate constants are corrected by multiplying the TST rate constants in the Wigner and Eckart tunneling correction factors. The Wigner tunneling correction [43] has been considered as follows:

$$\kappa_{\mathrm{Wigner}}(T) = 1 + \frac{1}{24}\left(\frac{h\ \mathrm{Im}(\nu^{\neq})}{k_{\mathrm{B}} T}\right)^2 \tag{2}$$

where Im($\nu^{\neq}$) is the imaginary vibrational frequency of the relevant transition state. Tunneling effects based on the unsymmetrical Eckart potential energy barrier [44] can be calculated by numerically integrating the probability $p(E)$ of transmission through the corresponding 1D barrier at energy E over a Boltzmann distribution of energies:

$$\kappa_{\mathrm{Eckart}}(T) = \frac{\exp\left(\Delta H_{\mathrm{f}}^{\neq,0\mathrm{K}} / k_{\mathrm{B}} T\right)}{k_{\mathrm{B}} T} \int_{\mathrm{o}}^{\infty} p(E) \exp\left(-E / k_{\mathrm{B}} T\right) \mathrm{d}E \tag{3}$$

where $\Delta H_{\mathrm{f}}^{\neq,0\mathrm{K}}$ is the zero-point corrected energy barrier in the forward direction. Uncorrected and corrected rate constants are fitted to the 3-parameters conventional Arrhenius (modified Arrhenius) equation.

Also, the thermal rate constants are calculated on a microcanonical basis from the standard RRKM expression [31-33] to evaluate pressure effects both in the fall-off regime and towards the high pressure limit along with the following equation:

$$k_{\mathrm{uni}}(T) = \frac{\sigma\, Q_1^{\neq}}{h\, Q_2\, Q_1} \exp(-E_{\mathrm{o}}/k_{\mathrm{B}}T) \int_0^{\infty} \frac{G(E)\exp(-E/k_{\mathrm{B}}T)}{1+\dfrac{k(E_{\mathrm{o}}+E+\langle \Delta E_j \rangle)}{\omega}}\, \mathrm{d}E \qquad (4)$$

In the above equation, $\langle \Delta E_j \rangle = (1-\frac{I^{\neq}}{I}) \times k_{\mathrm{B}}T$, $I^{\neq}$ and I are the average of the two largest moments of inertia, $G(E)$ is the total number of states of the transition state with energy less than or equal to E, E_{o} is the zero-point-corrected threshold energy, $Q_1^{\neq}$ and Q_1 are the partition functions for adiabatic rotations of the transition state and reactant respectively, and Q_2 is the partition function of the active degrees of freedom (vibrations + K-rotor) of the reactant, without rotational symmetry numbers. The strong collision approximation is used assuming that every collision deactivates with $\omega=\beta_{\mathrm{c}}.Z_{\mathrm{LJ}}.[\mathrm{M}]$ being the effective collision frequency, where β_{c} is the collisional efficiency, Z_{LJ} is the Lennard-Jones collision frequency and [M] is the total gas concentration. The collision frequencies (Z_{LJ}) were calculated using the Lennard-Jones parameters: $\varepsilon/k_{\mathrm{B}}$, which depends on the energy depth (ε) of the Lennard-Jones potential and σ, which represents a dimensional scale of the molecular radius. The retained Lennard-Jones potential parameters were σ = 3.465 Å, $\varepsilon/k_{\mathrm{B}}$ = 113.5 K for argon as diluent gas [45], and σ = 4.700 Å, $\varepsilon/k_{\mathrm{B}}$ = 393.1 K for $C_4H_6N_2$. For all RRKM calculations collisional efficiency β_{c} = 0.2 has been used. All supplied values for unimolecular kinetic rate constants are the results of calculations that were performed using the implementation of canonical transition state theory and statistical RRKM theory in the Kinetic and Statistical Thermodynamical Package (KiSThelP) by Canneaux *et al.* [46]. In all calculations a scaling factor of 0.956 was imposed on the calculated frequencies at the M06-2*x*/aug-cc-pVTZ level of theory [47].

Bonding changes along a reaction path can be studied from the characterization of the electron-density reorganization using bonding evolution theory (BET), consisting of the joint-use of ELF topology [1] and Thom's catastrophe theory (CT) proposed by Krokidis

et al. [48]. An orbital independent description of the electron localization can be described according to the Electron Localization Function (ELF) [48], which reads:

$$\mathrm{ELF} = \eta(\mathbf{r}) = \frac{1}{1+\left(D_\sigma / D_\sigma^0\right)^2} \tag{5}$$

ELF has values between 0 and 1 where 1 corresponds to a perfect localization, D_σ has the physical meaning of the excess of local kinetic energy density due to Pauli's repulsion, and D_σ^0 is the Thomas-Fermi kinetic energy density, which can be regarded as a renormalization factor [48]. A topological analysis of the ELF provides core basins and valence basins, which are the domains in which the probability of finding an electron pair is maximal. The valence basins are characterized according to their synaptic order that is the number of core basins sharing a boundary with the valence basin. Monosynaptic basins, labelled V(A), correspond to lone pairs or non-bonding regions, while disynaptic basins, labelled V(A,B), connect the core of two nuclei A and B and, thus, correspond to a bonding region between A and B [48, 49].

According to the type of attractor, the average population for a topological basin labeled Ω_i [50] is defined by:

$$\bar{N}(\Omega_i) = \int_{\Omega_i} \rho(\mathbf{r})\mathrm{d}\mathbf{r} \tag{6}$$

The topological analysis of the ELF was performed for all the selected structures along the reaction coordinate by means of the TopMod program [51] upon the calculated M06-2*x*/aug-cc-pVTZ wavefunctions.

Results and discussion:

An analysis of the reaction along the reaction coordinate indicates that breaking of two C–N single bonds takes place through a one-step process. The geometry of the TS involved in the cheletropic elimination of N_2 from (2,5-dihydro-1*H*-pyrrol-1-ium-1-ylidene) amide ($C_4H_6N_2$) is given in Fig. 1. The length of the breaking C–N single bonds, of the forming double C=C bonds, and of the C_2–C_3 bond at the TS are equal to 1.794, 1.433, and 1.359 Å, respectively.

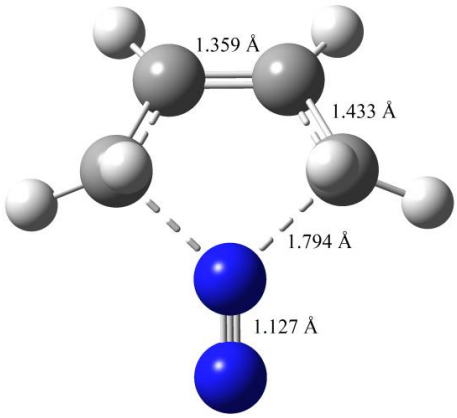

Fig. 1. M06-2*x*/aug-cc-pVTZ geometry of transition structure involved in the cheletropic elimination of N_2 from $C_4H_6N_2$.

The evaluation of the global electron-density transfer (GEDT) along the reaction is made using electrostatic Hirshfeld population analysis [52]. The Hirshfeld population analysis of the TS yields a GEDT flux of 0.041 ē from the nucleophilic 1,3-butadiene unit toward the electrophilic N_2 part, which shows that this reaction has a non-polar character. The predicted harmonic vibrational frequencies and rotational moments of inertia for the reactant and its TS are shown in Supporting Information (Table S1) and applied for calculating rate constants and other kinetic parameters. Relative enthalpies, entropies and Gibbs free energies of the stationary points involved in the cheletropic elimination of N_2 from $C_4H_6N_2$ are calculated at temperatures ranging from 300 to 900 K, and given in Supporting Information (Table S2).

All obtained temperature-dependent TST rate constants and fitted modified Arrhenius parameters for the cheletropic elimination of N_2 from $C_4H_6N_2$ are presented in Table 1. Further fall-off plot for the unimolecular rate constants (k_{uni}) as a function of pressure, high pressure limit of rate constants (k_∞), atmospheric rate constant (k^{1atm}), low pressure limit of rate constants (k_o), transition pressure ($P_{1/2}$) values and their Lennard-Jones collision frequency (Z_{LJ}) values at the same temperatures are computed by means of RRKM theory, and presented in Fig. 2 and Table 2.

Table 1. The temperature-dependent rate constants, tunneling corrections, and fitted modified Arrhenius parameters ($k=AT^n\exp[-E_a/RT]$) calculated by means of TST theory.

Tunneling	κ	T (K) ± 20%	k (s^{-1})	A (s^{-1})	n	E_a (kJ/mol)
-	-	300	3.5688×10^{6}	1.3567×10^{9}	1.372	34.32
	-	500	1.7460×10^{9}	3.6170×10^{10}	0.9011	35.86
	-	700	2.7662×10^{10}	5.5063×10^{11}	0.5312	37.64
	-	900	1.3289×10^{11}	2.7815×10^{12}	0.3195	39.00
Wigner	1.26	300	4.4849×10^{6}	2.2440×10^{8}	1.614	32.70
	1.09	500	1.9074×10^{9}	1.1722×10^{10}	1.046	34.55
	1.05	700	2.8967×10^{10}	2.7670×10^{11}	0.6164	36.62
	1.03	900	1.3668×10^{11}	1.7566×10^{12}	0.3742	38.17
Eckart	1.31	300	4.6589×10^{6}	9.3597×10^{6}	2.071	31.19
	1.10	500	1.9187×10^{9}	7.2589×10^{9}	1.110	34.20
	1.05	700	2.9024×10^{10}	2.4520×10^{11}	0.6319	36.49
	1.03	900	1.3692×10^{11}	2.1359×10^{12}	0.3494	38.33

The cheletropic elimination of N_2 from $C_4H_6N_2$ is an exothermic and spontaneous process (Supporting Information, Table S2) which present a low activation energy. The low activation energy and the strong exothermic character of the reaction together with the positive entropic effect make the $C_4H_6N_2$ compound thermally unstable, since it readily undergoes the elimination process. The supplied kinetic results using TST theory (Table 1) indicate that at a pressure of 1.0 atm the rate constants are positively dependent on the temperature and the tunneling effect on the reaction rate at the highest temperatures is negligible. Inspection of Fig. 2 and Table 2 shows that the RRKM unimolecular rate constants obtained for the reported reaction pathway increase with increasing temperatures. Upon inspecting the RRKM data displayed in Fig. 2, it appears quite clearly that at the temperatures 300, 500, 700 and 900 K, pressures larger than 10, 10^2, 10^3, and 10^4 atm are required for ensuring a saturation to the high pressure limit of the RRKM unimolecular rate constants, showing that transition state theory breaks down and the fall-off expression is necessary for the kinetic modeling. Upon applying RRKM theory over the temperature range 240–360 K and at 1 atm, the unimolecular rate constant can be evaluated as follows:

$$k^{1.0\,\mathrm{atm}}_{(240-360\ \mathrm{K})} = 1.0249 \times 10^{12} \times \mathrm{e}^{-\frac{33.11\ \mathrm{kJ/mol}}{RT}} \quad \mathrm{s}^{-1}$$

This reaction is going to be incredibly fast at room temperature, and indeed, the RRKM rate constant corresponds to a lifetime 6×10^{-7} s for $C_4H_6N_2$ at ambient conditions. Transition pressure values show that the unimolecular rate constants of the cheletropic elimination reaction at atmospheric pressure and the lower pressures of the troposphere are in the fall-off regimes.

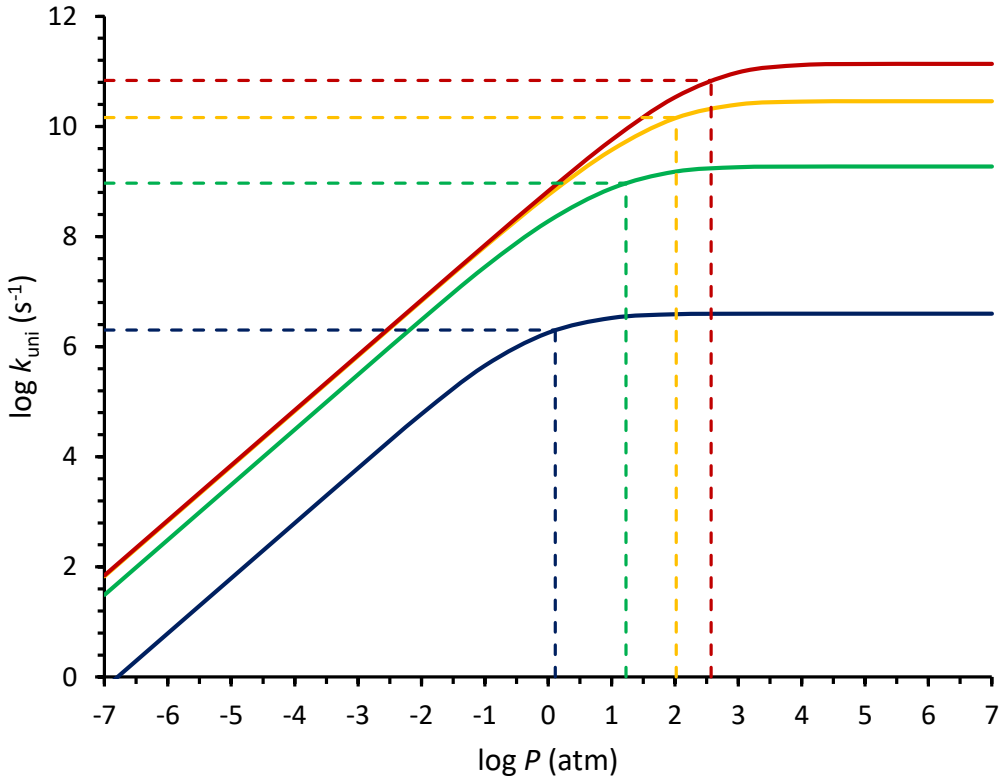

Fig. 2. Fall-off plots for the rate constants as a function of pressure at 300 (blue line), 500 (green line), 700 (yellow line), and 900 (red line) K calculated by means of RRKM theory with relative collision efficiency $\beta_c = 0.2$. Fall-off regions are separated by dashed lines.

Table 2. High pressure rate constant (k_∞), atmospheric rate constant (k^{1atm}), low pressure rate constant (k_o), Lennard-Jones collision frequency (Z_{LJ}), and transition pressure ($P_{1/2}$) calculated by means of RRKM theory.

T (K) ± 20%	k_∞ (s^{-1})	k^{1atm} (s^{-1})	k_o (cm^3 $molecule^{-1}$ s^{-1})	Z_{LJ} (cm^3 $molecule^{-1}$ s^{-1})	$P_{1/2}$ (atm)
300	3.9934×10^{6}	1.7955×10^{6}	2.55×10^{-13}	3.52×10^{-10}	1.29
500	1.8604×10^{9}	1.8798×10^{8}	2.11×10^{-11}	3.87×10^{-10}	16.96
700	2.8783×10^{10}	5.6910×10^{8}	6.46×10^{-11}	4.18×10^{-10}	104.96
900	1.3674×10^{11}	6.6638×10^{8}	8.59×10^{-11}	4.44×10^{-10}	371.53

The BET study of the cheletropic elimination of N_2 from (2,5-dihydro-1*H*-pyrrol-1-ium-1-ylidene) amide ($C_4H_6N_2$) indicates that this reaction along the intrinsic reaction coordinate can be topologically divided into four differentiated phases. The reaction path calculated by means of the IRC method together with the relative position of seven selected points is shown in Fig. 3. The population of the most relevant ELF valence basins of the reactant (**R**), products (**P**) and the seven selected points ($\mathbf{P_i}$; i=1–7) along the reaction coordinate are presented in Table 3. Lewis representation of bonding changes along the selected points is given in Fig. 4; the ELF attractor positions for the most relevant points along the IRC and the disynaptic basin population changes along the reaction path are shown in Supporting Information (Figs. S1 and S2).

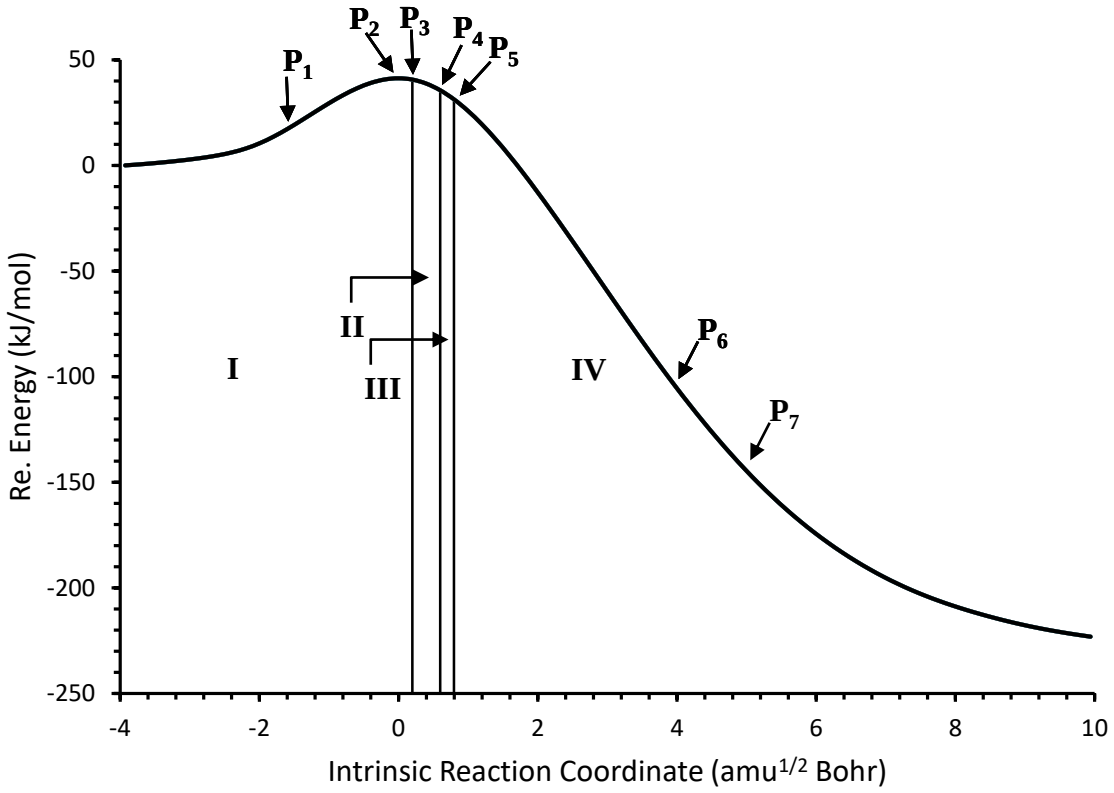

Fig. 3. Schematic representation of the energy profiles for the cheletropic elimination of N_2 from $C_4H_6N_2$ calculated by means of the IRC method, with a step size of 0.1 $amu^{1/2}$ Bohr. The selected points of the IRC are considered for the ELF topological analysis.

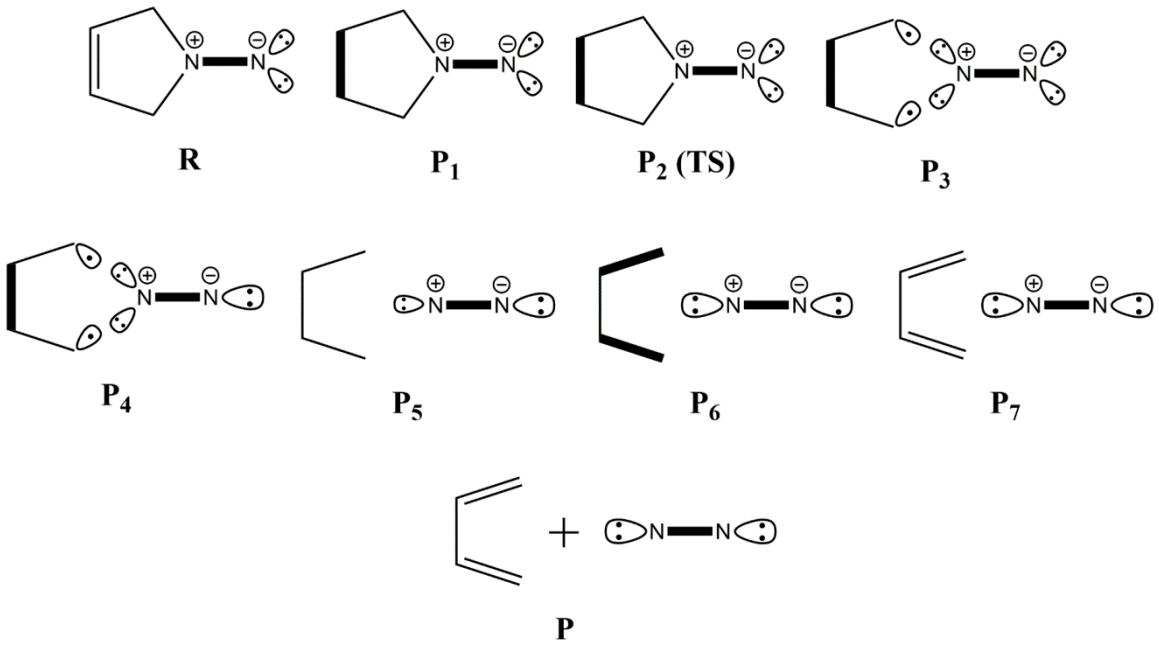

Fig. 4. The disynaptic [lines; V(X,Y)] and monosynaptic basins [ellipses with a dot and two dots; V(X)] at the selected points involved in the cheletropic elimination of N_2 from $C_4H_6N_2$ from the perspective of the ELF analysis. Filled lines, and large ellipses with two dots indicate disynaptic and lone electron pairs monosynaptic basins with a population larger than 3.0 ē, respectively.

Phase **I**, 1.526 ≤ *d* C–N (Å) < 1.818, begins from $C_4H_6N_2$ (**R**) and ends before **P₃** point. At the reactant position, *d* C–N=1.526 Å and a significant GEDT equal to 0.169 ē takes place from the diene fragment to N_2. The ELF topological analysis of **R** shows two disynaptic basins V (C_1–C_2) and V (C_3–C_4), integrating to 2.04 ē, which are associated with the C_1–C_2 and C_3–C_4) single bonds; two disynaptic basins V (C_2–C_3) and V′ (C_2–C_3) with a population of 1.72 and 1.73 ē, which are associated with the C_2=C_3 double bond; two disynaptic basins V (C_1–N_5) and V (C_4–N_5), with a population integrating to 1.87 ē, which are associated with the C_1–N_5 and C_4–N_5 single bonds; and one disynaptic basin V (N_5–N_6), with a population integrating to 3.31 ē, which is associated with the N_5=N_6 double bond. In addition, two monosynaptic basins V (N_6) and V′ (N_6), with electron populations of 2.21 ē are associated with the two lone pairs of N_6. At **P₁** of the

IRC, *d* C–N=1.771 Å, two disynaptic basins associated with the C_2=C_3 double bond merge into one disynaptic basin V (C_2–C_3) with an electron population 3.39 ē, and GEDT has decreased to 0.126 ē. The transition state of the reaction (**P2** point) is located in this phase at *d* C–N=1.795 Å. At this point, the population of the disynaptic basins V (C_1–C_2) and V (C_3–C_4) have increased to 2.38 ē, whereas the population of the disynaptic basins V (C_2–C_3), V (C_1–N_5), V (C_4–N_5) and V (N_5–N_6) have decreased continuously to 3.21, 1.75, 1.75 and 3.34 ē, respectively. The populations of the two monosynaptic basins V (N_6) and V′ (N_6) have decreased to 1.93 yielding an integrated population of 3.86 ē. These changes in basin populations at **P2** point (TS) are associated with a GEDT equal to 0.041 ē from the diene framework. Additional information about the nature of bonding in the transition state may be deduced from discrimination between basins by the reduction of reducible domains. In Fig. 5 the tree reduction diagram (bifurcation graph) of ELF localization domains shows the hierarchy of ELF basin domains.

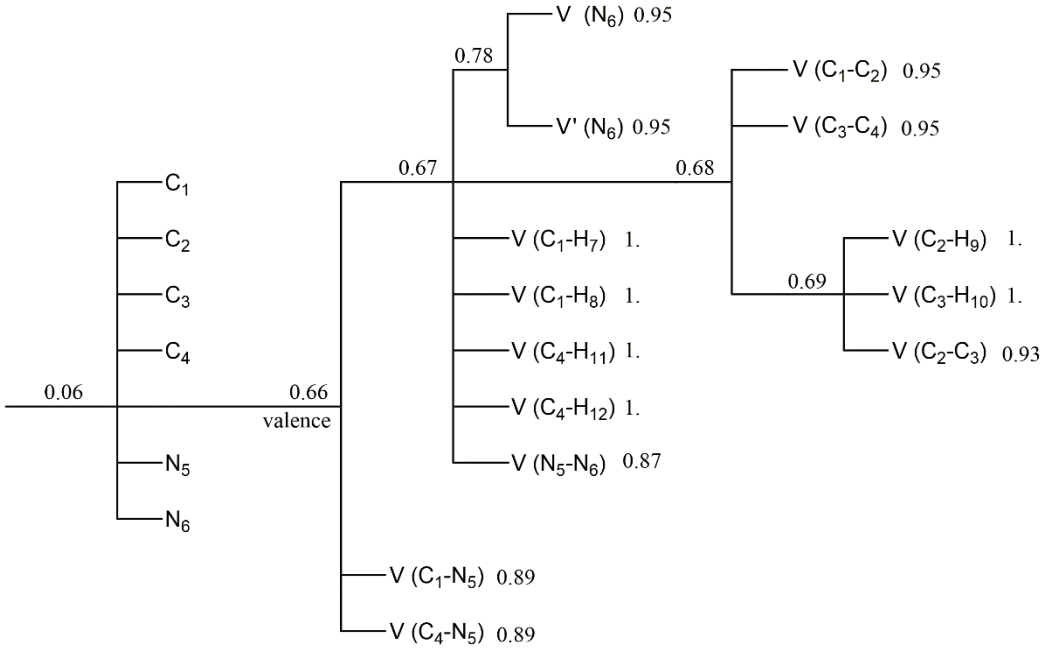

Fig. 5. Reduction tree diagrams of ELF localization domains for the transition structure.

Table 3. Integrated electron populations for valence ELF basins at some selected points of IRC. *d* C–N stands for the distance (Å) between C_1 or C_4 atom of diene and N_5 atom. C (N_5) and C (N_6) are local charges (ē) on N_5 and N_6 atoms, respectively. The GEDT is the global electron-density transfer (ē).

	R	P_1	P_2 (TS)	P_3	P_4	P_5	P_6	P_7	P
d C–N	1.526	1.771	1.795	1.818	1.867	1.891	2.279	2.375	
C (N_5)	0.092	0.099	0.105	0.104	0.102	0.101	0.071	0.066	
C (N_6)	-0.261	-0.225	-0.146	-0.135	-0.113	-0.104	-0.034	-0.028	
GEDT	0.169	0.126	0.041	0.031	0.011	0.003	-0.037	-0.038	
V (C_1–C_2) [a]	2.04	2.11	2.38	2.44	2.59	2.83	3.24	1.58	1.58
V′ (C_1–C_2) [a]								1.70	1.79
V (C_2–C_3)	1.72	3.39	3.21	3.17	3.05	2.97	2.32	2.28	2.16
V′ (C_2–C_3)	1.73								
V (C_1–N_5) [a]	1.87	1.80	1.75						
V (C_1)				0.28	0.19				
V (N_5–N_6)	3.31	3.38	3.34	3.35	3.40	3.42	3.63	3.66	3.64
V (N_5)				1.46	1.47	2.95	3.04	3.04	3.08
V′ (N_5)				1.46	1.47				
V (N_6)	2.21	2.13	1.93	1.90	3.65	3.60	3.18	3.15	3.08
V′ (N_6)	2.21	2.13	1.93	1.90					

[a] Due to the symmetry of molecule, ELF populations of V (C_1–C_2) and V′ (C_1–C_2) at the selected points are equal to V (C_3–C_4) and V′ (C_3–C_4); and ELF populations of V (C_1–N_5) at the selected points are equal to V (C_4–N_5).
[b] Atom numbering is given in scheme 2.

In the transition state there are six core attractors, labeled C (C_i) and C (N_i), six protonated disynaptic attractors, V (C_i,H_j), two monosynaptic attractors V (N_6) and V′ (N_6), and six disynaptic attractors V (C_1–C_2), V (C_2–C_3), V (C_3–C_4), V (C_1–N_5), V (C_4–N_5), and V (N_5–N_6). At **P₂** point (TS), the first partition into core and valence basins occurs for η(**r**) = 0.06. After the core-valence isolation, the valence domain undergoes a second separation into three domains at η(**r**) = 0.66. These domains correspond to the V (C_1–N_5) and V (C_4–N_5), with ELF values around 0.89, and remainder of the structure. The remainder of the structure is reduced at η(**r**) = 0.67 into four protonated reducible domains V (C_1–H_7), V (C_1–H_8), V (C_4–H_{11}), V (C_4–H_{12}), with ELF values 1; one V (N_5–N_6) domain, with an ELF value around 0.87; and two rest domains. One of the rest domains is split at η(**r**) = 0.68 into V (C_1–C_2) and V (C_3–C_4) domains, with ELF values 0.95. The next reduction of this domain into two protonated reducible domains V (C_2–H_9) and V (C_3–H_{10}), with ELF values equal to 1, and V (C_2-C_3) domain, with ELF values around 0.93, occurs at η(**r**) = 0.69. The other rest domain is split at η(**r**) = 0.78 into two V (N_6) and V′ (N_6) domains, with ELF values around 0.95.

Phase **II**, 1.818 ≤ *d* C–N (Å) < 1.867, begins from **P₃** point and ends before **P₄** point. The most significant topological change along the reaction coordinate takes place in this phase. At **P₃** point, *d* C–N=1.818 Å, two disynaptic basins V (C_1–N_5) and V (C_4–N_5) associated with the C_1–N_5 and C_4–N_5 single bonds disappear, which indicates that cleavage of C_1–N_5 and C_4–N_5 single bonds have already begun. Depopulation of two disynaptic basins V (C_1–N_5) and V (C_4–N_5) leads to the formation of two monosynaptic basins V (N_5) and V′ (N_5), associated with the two lone pairs at the N_5 (with electron populations equal to 1.46 ē, integrating to 2.92 ē); and to the formation of two monosynaptic basin V (C_1) and V (C_4) at the terminal C_1 and C_4, integrating to 0.28 ē. In addition to this, the electronic populations of disynaptic basins V (C_1–C_2), V (C_3–C_4) and V (N_5–N_6) increase to 2.44, 2.44 and 3.35 ē, respectively. On the other hand, the electronic populations of the disynaptic basin V (C_2–C_3) and monosynaptic basins V (N_6) and V′ (N_6) decrease to 3.17, 1.90 and 1.90 ē, respectively. At this point, GEDT decreases to 0.031 ē.

Phase **III**, 1.867 ≤ *d* C–N (Å) < 1.891, starts at **P$_4$** point and ends before **P$_5$** point. At the **P$_4$** point, *d* C–N=1.867 Å, two monosynaptic basins V (N_6) and V′ (N_6) are merged into one monosynaptic basin V (N_6) which presents a population of 3.65 ē. Additionally, the population of disynaptic basins V (C_1–C_2), V (C_3–C_4), V (N_5–N_6) and monosynaptic basins V (N_5), V′ (N_5) are increased to 2.59, 2.59, 3.40, 1.47, and 1.47 ē, respectively, while disynaptic basin V (C_2–C_3) and monosynaptic basins V (C_1) and V (C_4) are decreased to 3.05, 0.19 and 0.19 ē, respectively. These changes in basin populations are associated with a GEDT equal to 0.011 ē.

Phase **IV**, 1.891 ≤ *d* C–N (Å) < 2.375, begins at **P$_5$** point and ends at products (**P**). There are two important changes at **P$_5$** point, *d* C–N=1.891 Å, i) the electronic population of disynaptic basins V (C_1–C_2) and V (C_3–C_4) greatly increase to 2.83 ē, which are as a result of the depopulation and disappearing of monosynaptic basins V (C_1) and V (C_4); and ii) the merging of two monosynaptic basins V (N_5) and V′ (N_5) into one monosynaptic basin V (N_5), which integrates to a population of 2.95 ē.

Increasing in the population of the disynaptic basins V (C_1–C_2) and V (C_3–C_4) at this phase are associated to the formation of the C_1=C_2 and C_3=C_4 double bonds.

At **P$_6$** point the population of the V (C_1–C_2), V (C_3–C_4) disynaptic and V (N_5) monosynaptic basins exceed than 3 ē. Finally, at **P$_7$** point, *d* C–N=2.375 Å, the V (C_1–C_2) and V (C_3–C_4) disynaptic basins split into two pairs V (C_1–C_2), V′ (C_1–C_2) and V (C_3–C_4), V′ (C_3–C_4) disynaptic basins, which integrate to 1.58, 1.58 and 1.70, 1.70 ē, respectively. At this point the populations of the disynaptic basin V (C_2–C_3) and of the monosynaptic basin V (N_6) have decreased to 2.28 and 3.15 ē, respectively, while the population of the disynaptic basin V (N_5–N_6) has increased up to 3.66 ē. On the other hand, the population of the monosynaptic basin V (N_5) remains equal to 3.04 ē. With the formation of C_1=C_2 and C_3=C_4 double bonds and C_2–C_3 single bond, GEDT changes until reaching a slightly negative value -0.038 ē at **P$_7$** point, as the consequence of a back donation process. From **P$_7$** to products (**P**) only changes in the basin populations occur. BET analysis along the reaction path indicates that cheletropic elimination reaction takes place along four topologically differentiated successive structural stability domains

(SSDs), which corresponds to the $C_4H_6N_2$: 4-[$\mathbf{C}^{\dagger}\mathbf{C}^{\dagger}$] **F** [**FFF**]-0: C_4H_6 + N_2 sequence of catastrophes.

Conclusions

The cheletropic elimination process of N_2 from (2,5-dihydro-1*H*-pyrrol-1-ium-1-ylidene) amide ($C_4H_6N_2$) has been studied computationally using density functional theory along with M06-2*x* exchange-correlation functional and an extremely large basis set (aug-cc-pVTZ). Kinetic rate constants were correspondingly estimated in the high pressure limit by means of transition state theory, on the grounds of partition functions calculated using the rigid rotor-harmonic oscillator approximation. Their pressure dependence has been investigated by means of statistical Rice–Ramsperger–Kassel–Marcus (RRKM) theory in the pressure range 10^{-7}–10^{7} atm and at temperatures equal to 300, 500, 700, and 900 K. Energetically, elimination of N_2 from $C_4H_6N_2$ is exothermic and exoergic with a low activation energy, around 33 kJ/mol. The tunneling factor at ambient temperature is ~1.3, while at higher studied temperatures this factor becomes negligible. Fall-off curve regimes indicate that the transition-state-approximation breaks down for the studied unimolecular reaction. The RRKM unimolecular rate constant of the cheletropic elimination at 300 K and 1 atm is equal to 1.7986× 10^{6} s^{-1}. Its temperature dependence at this level of theory can be described as follows:

$$k^{1.0\ \mathrm{atm}}_{(240-360\ \mathrm{K})} = 1.0249\times10^{12}\exp\left(-\frac{33.11\ \mathrm{kJ/mol}}{RT}\right)\ \mathrm{s}^{-1}$$

In the following, bond forming/breaking processes along the cheletropic elimination of N_2 from $C_4H_6N_2$ have been analyzed based on bonding evolution theory (BET) using an electron localization function (ELF) of the most relevant points. ELF topological analysis reveals that the cheletropic elimination process takes place along four topologically differentiated SSDs associated to the sequence of catastrophes 4-[$\mathbf{C}^{\dagger}\mathbf{C}^{\dagger}$] **F** [**FFF**]-0: C_4H_6 + N_2. Breaking of C–N bonds and the other selected points separating the SSDs along the reaction coordinate are in the vicinity of the TS at Rx range 0.1992-0.7966 $amu^{1/2}$Bohr.

Supporting information

Supporting information file is available with the article through the journal web site at XXX.

Acknowledgments

The authors thank anonymous referees for highly relevant comments. E. Zahedi expresses his gratitude to the Islamic Azad University, Shahrood Branch.

References:

[1] A.D. Becke, K.E. Edgecombe, A simple measure of electron localization in atomic and molecular systems, *J. Chem. Phys.*, **92**, 5397-5403 (1990).

[2] B. Silvi, A. Savin, Classification of chemical bonds based on topological analysis of electron localization functions, *Nature*, **371**, 683-686 (1994).

[3] S. Berski, J. Andrés, B. Silvi, L.R. Domingo, The joint use of catastrophe theory and electron localization function to characterize molecular mechanisms. A density functional study of the Diels-Alder reaction between ethylene and 1,3-butadiene, *J. Phys. Chem. A*, **107**, 6014-6024 (2003).

[4] V. Polo, J. Andrés, A joint study based on the electron localization function and catastrophe theory of the chameleonic and centauric models for the Cope rearrangement of 1,5-hexadiene and its cyano derivatives, *J. Comput. Chem.*, **26**, 1427-1437 (2005).

[5] V. Polo, J. Andrés, S. Berski, L.R. Domingo, B. Silvi, Understanding reaction mechanisms in organic chemistry from catastrophe theory applied to the electron localization function topology, *J. Phys. Chem. A*, **112**, 7128-7136 (2008).

[6] S. Berski, J. Andrés, B. Silvi, L.R. Domingo, New findings on the Diels-Alder reactions. An analysis based on the bonding evolution theory, *J. Phys. Chem. A*, **110**, 13939-13947 (2006).

[7] M. Ríos-Gutiérrez, L.R. Domingo, P. Pérez, Understanding the high reactivity of carbonyl compounds towards nucleophilic carbenoid intermediates generated from carbene isocyanides, *RSC Adv.*, **5**, 84797-84809 (2015).

[8] L.R. Domingo, P. Pérez, J.A. Sáez, Understanding the regioselectivity in hetero DielseAlder reactions. An ELF analysis of the reaction between nitrosoethylene and 1-vinylpyrrolidine, *Tetrahedron*, **69**, 107-114 (2013).

[9] L.R. Domingo, P. Pérez, J.A. Sáez, Understanding C–C bond formation in polar reactions. An ELF analysis of the Friedel–Crafts reaction between indoles and nitroolefins, *RSC Adv.*, **3**, 7520-7528 (2013).

[10] L.R. Domingo, M.J. Aurella, P. Pérez, The mechanism of ionic Diels–Alder reactions. A DFT study of the oxa-Povarov reaction, *RSC Adv.*, **4**, 16567-16577 (2014).

[11] L.R. Domingo, A new C–C bond formation model based on the quantum chemical topology of electron density, *RSC Adv.*, **4**, 32415-32428 (2014).

[12] L.R. Domingo, J.A. Sáez, Understanding the selectivity in the formation of δ-lactams vs. β-lactams in the Staudinger reactions of chloro-cyan-ketene with unsaturated imines. A DFT study, *RSC Adv.*, **4**, 58559–58566 (2014).

[13] L.R. Domingo, M. Ríos-Gutiérrez, P. Pérez, Unravelling the mechanism of the ketene-imine Staudinger reaction. An ELF quantum topological analysis, *RSC Adv.*, **5**, 37119-37129 (2015).

[14] L.R. Domingo, M.J. Aurella, P. Pérez, Understanding the polar mechanism of the ene reaction. A DFT study, *Org. Biomol. Chem.*, **12**, 7581-7590 (2014).

[15] L.R. Domingo, M. Ríos-Gutiérrez, P. Pérez, A DFT study of the ionic [2+2] cycloaddition reactions of keteniminium cations with terminal acetylenes, *Tetrahedron*, **71**, 2421-2427 (2015).

[16] P. Pérez, L.R. Domingo, A DFT study of inter- and intramolecular aryne ene reactions, *Eur. J. Org. Chem.*, **2015**, 2826-2834 (2015).

[17] A.K. Nacereddine, C. Sobhi, A. Djerourou, M. Ríos-Gutiérrez, L.R. Domingoc, Non-classical CH/O hydrogen-bond determining the regio- and stereoselectivity in the [3+2] cycloaddition reaction of (Z)-C-phenyl-Nmethylnitrone with dimethyl 2-benzylidenecyclopropane-1,1-dicarboxylate. A topological electron-density study, *RSC Adv.*, **5**, 99299-99311 (2015).

[18] V. Polo, L.R. Domingo, J. Andrés, Better understanding of the ring-cleavage process of cyanocyclopropyl anionic derivatives. A theoretical study based on the electron localization function, *J. Org. Chem.*, **71**, 754-762 (2006).

[19] L.R. Domingo, E. Chamorro, P. Pérez, Understanding the mechanism of non-polar Diels-Alder reactions. A comparative ELF analysis of concerted and stepwise diradical mechanisms, *Org. Biomol. Chem.*, **8**, 5495-5504 (2010).

[20] L.R. Domingo, Why Diels-Alder reactions are non-concerted processes?, *J. Chil. Chem. Soc.*, **59**, 2615-2618 (2014).

[21] E.V. Anslyn, D.A. Dougherty, Modern Physical Organic Chemistry, University Science Books, United States of America, 2006.

[22] J.P. Buxton, C.J.S.M. Simpson, Thermal decarbonylations of unsaturated cyclic ketones: Kinetics and dynamics, *Chem. Phys.*, **105**, 307-316 (1986).

[23] D.M. Birney, S. Ham, G.R. Unruh, Pericyclic and pseudopericyclic thermal cheletropic decarbonylations: When can a pericyclic reaction have a planar, pseudopericyclic transition state?, *J. Am. Chem. Soc.*, **119**, 4509-4517 (1997).

[24] N.S. Isaacs, A.A.R. Laila, Rates of addition of sulphur dioxide to some 1,3-dienes *Tetrahedron Lett.*, **17**, 715-716 (1976).

[25] D. Suárez, E. Iglesias, T.L. Sordo, J.A. Sordo, Mechanism of cheletropic reactions of 1,3-dienes with sulfur dioxide, *J. Phys. Org. Chem.*, **9**, 17-20 (1996).

[26] D.L. Lemal, S.D. McGregor, Dienes from 3-pyrrolines. A stereospecific deamination, *J. Am. Chem. Soc.*, **88**, 1335-1336 (1966).

[27] H. Eyring, The activated complex and the absolute rate of chemical reactions, *Chem. Rev.*, **17**, 65-77 (1935).

[28] D.G. Truhlar, B.C. Garrett, S.J. Klippenstein, Current status of transition-state theory, *J. Phys. Chem.*, **100**, 12771-12800 (1996).

[29] A. Fernandez-Ramos, B.A. Ellingson, B.C. Garrett, D.G. Truhlar, Variational transition state theory with multidimensional tunneling, *Rev. Comput. Chem.*, **23**, 125-232 (2007).

[30] W. Forst, Unimolecular rate theory test in thermal reactions, *J. Phys. Chem.*, **76**, 342-348 (1972).

[31] W. Forst, Unimolecular Reactions. A Concise Introduction, C. U. Press, Cambridge, 2003.

[32] P.J. Robinson, K.A. Holbrook, Unimolecular Reactions, Wiley-Interscience, New York, 1972.

[33] K.A. Holbrook, M.J. Pilling, S.H. Robertson, Unimolecular Reactions, 2nd ed., Wiley, Chichester, 1996.

[34] M.J. Frisch, G.W. Trucks, H.B. Schlegel, G.E. Scuseria, M.A. Robb, J.R. Cheeseman, G. Scalmani, V. Barone, B. Mennucci, G.A. Petersson, H. Nakatsuji, M. Caricato, X. Li, H.P. Hratchian, A.F. Izmaylov, J. Bloino, G. Zheng, J.L. Sonnenberg, M. Hada, M. Ehara, K. Toyota, R. Fukuda, J. Hasegawa, M. Ishida, T. Nakajima, Y. Honda, O. Kitao, H. Nakai, T. Vreven, J.A. Montgomery-Jr., J.E. Peralta, F. Ogliaro, M. Bearpar, J.J. Heyd, E. Brothers, K.N. Kudin, V.N. Staroverov, R. Kobayashi, J. Normand, K. Raghavachari, A. Rendell, J.C. Burant, S.S. Iyengar, J. Tomasi, M. Cossi, N. Rega, J.M. Millam, M. Klene, J.E. Knox, J.B. Cross, V. Bakken, C. Adamo, J. Jaramillo, R. Gomperts, R.E. Stratmann, O. Yazyev, A.J. Austin, R. Cammi, C. Pomelli, J.W. Ochterski, R.L. Martin, K. Morokuma, V.G. Zakrzewski, G.A. Voth, P. Salvador, J.J. Dannenberg, S. Dapprich, A.D. Daniels, O. Farkas, J.B. Foresman, J.V. Ortiz, J. Cioslowski, D.J. Fox, Gaussian 09, Revision A.02-SMP., in, Gaussian, Inc. , Wallingford CT, 2009.

[35] X. Li, M.J. Frisch, Energy-represented DIIS within a hybrid geometry optimization method, *J. Chem. Theory Comput.*, **2**, 835-839 (2006).

[36] Y. Zhao, D.G. Truhlar, The M06 suite of density functionals for main group thermochemistry, thermochemical kinetics, noncovalent interactions, excited states, and transition elements: Two new functionals and systematic testing of four M06 functionals and twelve other functionals, *Theor. Chem. Acc.*, **120**, 215-241 (2008).

[37] Y. Zhao, D.G. Truhlar, Density functionals with broad applicability in chemistry, *Acc. Chem. Res.*, **41**, 157-167 (2008).

[38] T.H. Dunning-Jr., Gaussian basis sets for use in correlated molecular calculations. I. The atoms boron through neon and hydrogen, *J. Chem. Phys.*, **90**, 1007-1023 (1989).

[39] H.P. Hratchian, H.B. Schlegel, Accurate reaction paths using a Hessian based predictor-corrector integrator, *J. Chem. Phys.*, **120**, 9918-9924 (2004).

[40] H.P. Hratchian, H.B. Schlegel, Theory and Applications of Computational Chemistry: The First 40 Years, Elsevier, Amsterdam, 2005.

[41] H.P. Hratchian, H.B. Schlegel, Using Hessian updating to increase the efficiency of a Hessian based predictor-corrector reaction path following method, *J. Chem. Theory Comput.*, **1**, 61-69 (2005).

[42] J.I. Steinfeld, J.S. Francisco, W.L. Hase, Chemical Kinetics and Dynamics, 2nd ed., Prentice-Hall, Inc., New Jersey, USA, 1999.

[43] E. Wigner, Über das überschreiten von potentialschwellen bei chemischen reaktionen, *Z. Phys. Chem. Abt. B*, **19**, 203-216 (1932).

[44] C. Eckart, The penetration of a potential barrier by electrons, *Phys. Rev.*, **35**, 1303-1309 (1930).

[45] F.M. Mourits, F.H.A. Rummens, A critical evaluation of Lennard-Jones and Stockmayer potential parameters and of some correlation methods, *Can. J. Chem.*, **55** 3007-3020 (1977).

[46] S. Canneaux, F. Bohr, E. Henon, KiSThelP: Kinetic and Statistical Thermodynamical Package, 2014.

[47] Computational chemistry comparison and benchmark dataBase, Precomputed vibrational scaling factors, http://cccbdb.nist.gov/vibscalejust.asp.

[48] X. Krokidis, S. Noury, B. Silvi, Characterization of elementary chemical processes by catastrophe theory, *J. Phys. Chem. A*, **101**, 7277-7282 (1997).

[49] L.R. Domingo, P. Pérez, A quantum chemical topological analysis of the C–C bond formation in organic reactions involving cationic species, *Phys. Chem. Chem. Phys.*, **16**, 14108-14115 (2014).

[50] A. Savin, B. Silvi, F. Colonna, Topological analysis of the electron localization function applied to delocalized bonds, *Can. J. Chem.*, **74**, 1088-1096 (1996).

[51] S. Noury, X. Krokidis, F. Fuster, B. Silvi, TopMod package, 1997.

[52] F.L. Hirshfeld, Bonded-atom fragments for describing molecular charge densities, *Theor. Chem. Acc.*, **44**, 129138 (1977).